PHYSICAL REVIEW APPLIED **10,** 044044 (2018)

High-Speed Neutron Imaging Using a Current-Biased Delay-Line Detector of Kinetic Inductance

Hiroaki Shishido,[1,2,*] Yuya Miki,[1] Hiroyuki Yamaguchi,[1] Yuki Iizawa,[1] Vu The Dang,[1,†]
Kenji M. Kojima,[3,4,5,‡] Tomio Koyama,[5] Kenichi Oikawa,[6] Masahide Harada,[6] Shigeyuki Miyajima,[7]
Mutsuo Hidaka,[8] Takayuki Oku,[6] Kazuhiko Soyama,[6] Soh Y. Suzuki,[9] and Takekazu Ishida[1,2,5]

[1] *Department of Physics and Electronics, Graduate School of Engineering, Osaka Prefecture University, Sakai, Osaka 599-8531, Japan*
[2] *NanoSquare Research Institute, Osaka Prefecture University, Sakai, Osaka 599-8531, Japan*
[3] *Muon Science Laboratory and Condensed Matter Research Center, Institute of Materials Structure Science, High Energy Accelerator Research Organization (KEK), Tsukuba, Ibaraki 305-0801, Japan*
[4] *Department of Materials Structure Science, The Graduate University for Advanced Studies, Tsukuba, Ibaraki 305-0801, Japan*
[5] *Division of Quantum and Radiation Engineering, Osaka Prefecture University, Sakai, Osaka 599-8570, Japan*
[6] *Materials and Life Science Division,*
J-PARC Center, Japan Atomic Energy Agency, Tokai, Ibaraki 319-1195, Japan
[7] *Advanced ICT Research Institute, National Institute of Information and Communications Technology, 588-2 Iwaoka, Nishi-ku, Kobe, Hyogo 651-2492, Japan*
[8] *Advanced Industrial Science and Technology, Tsukuba, Ibaraki 305-8568, Japan*
[9] *Computing Research Center, Applied Research Laboratory, High Energy Accelerator Research Organization (KEK), Tsukuba, Ibaraki 305-0801, Japan*

(Received 20 July 2018; published 17 October 2018)

We demonstrate the development of a high-speed neutron-imaging system via a solid-state superconducting detector. Our developed system, a current-biased kinetic-inductance detector (CBKID), operates in a delay-line mode to identify the position of a local hot spot in terms of four different arrival time stamps at the ends of the delay lines. Our detector comprises X and Y superconducting Nb meander lines, which are fed by a weak dc current, and a ^{10}B conversion layer, which converts a neutron into two charged particles. The high-energy light ions (^{4}He or ^{7}Li) in the $^{10}\mathrm{B}(n,\alpha)^7\mathrm{Li}$ reaction are able to create two hot spots simultaneously in the X and Y meanders. A pair of electromagnetic-wave pulses are generated at the hot spot and signals of different polarities start propagating on each of the X and Y meanders toward the ends. The position of the original hot spot is determined by the difference in arrival time of the two pulses at the two ends. To measure the arrival times of the pulse signals, we developed a set of analog signal discriminators from the preset threshold levels using a time-to-digital converter (TDC), which is able to record the timing of the propagated pulses with 1-ns resolution over a time frame of 4.2 s. We successfully reconstructed the neutron image of a test pattern with a spatial resolution of 22 μm and a detection rate tolerance of a few 10 MHz/cm^2.

DOI: 10.1103/PhysRevApplied.10.044044

I. INTRODUCTION

A neutron beam is useful for both scientific research and in various applications. It has a unique feature of high penetration into most materials except for some neutron absorbing/recoiling atoms, including those of hydrogen, lithium, and boron. Because a neutron has a magnetic dipole moment, it is also sensitive to local magnetic fields from the magnetic domains in a ferromagnet or more generally to any magnetic ordering in condensed matter. Neutron imaging is one promising application of neutron beams, and has extensively been developed to date in areas such as nondestructive transmission imaging, tomography, dark-field imaging, and visualization of the magnetic distribution in various materials [1], including intermetallic alloys [2], fuel cells

---

[*] shishido@pe.osakafu-u.ac.jp

[†] Present address: Materials and Life Science Division, J-PARC Center, Japan Atomic Energy Agency, Tokai, Ibaraki 319-1195, Japan.

[‡] Present address: Centre for Molecular and Materials Science, TRIUMF, 4004 Wesbrook Mall, Vancouver, British Columbia V6T 0A2, Canada.

[3], lithium ion batteries [4], and culturally significant artifacts [5].

Recent progress in the development of intensive neutron sources and the required peripheral equipment has made it possible to perform energy-resolved as well as high-spatial-resolution neutron imaging and tomography simultaneously [6]. Much effort has been devoted to develop a neutron imager with high spatial and temporal resolution. A high spatial resolution of 5.4 μm was recorded by using the color-center formation in LiF crystals [7] in a cold neutron beamline. Crystals exposed to neutrons were examined by a high-magnification microscope after irradiation. However, this method is not applicable to energy-resolved imaging by a pulsed neutron source because of its *ex situ* nature. A recent version of this approach that uses a gadolinium-gallium-garnet-(GGG-)scintillator-based neutron detector with a cooled CCD camera has reached a spatial resolution of 11 μm by optical magnification using cold neutrons at the reactor source [8]. Because *ex situ* reading by the CCD is required, this method is not applicable to a pulsed source. A high spatial resolution of 5.4 μm has also been achieved by an isotopically enriched gadolinium-oxysulfide scintillator screen combined with a dedicated magnifying objective and CCD detector in a cold neutron beamline [9]. Very recently, the highest reported spatial resolution of 2 μm was achieved by a gadolinium-oxysulfide-scintillator camera detector with a reactor source [10]. The scintillation light image was magnified by an optical microscope and imaged by a cooled sCMOS camera from Andor Technology. The center-of-mass calculation was applied to the scintillation events, resulting in a high-spatial-resolution image. One of the best candidates so far for use in a high spatial- and energy-resolution neutron imager is a multichannel plate (MCP). Tremsin *et al*. [2,11,12] have developed a ^{10}B-doped MCP combined with a Timepix readout [13] as a neutron imager. The nuclear reaction $^{10}\mathrm{B}(n,\alpha)^{7}\mathrm{Li}$, which emits a 0.84-MeV ^{7}Li ion and a 1.47-MeV ^{4}He ion as the dominant reaction channel, is converted into pulsed electrons and amplified in the ^{10}B-doped MCP. The signal is further amplified electronically and is read out by the Timepix sensor array, achieving a high spatial resolution of 55 μm. By using a center-of-gravity method, a higher spatial resolution of 10 μm is achieved with a sacrifice in the detection-rate tolerance, which decreased from GHz down to 3 MHz due to the computational time. A new chip, Timepix3, has been considered to overcome the previous count-rate limitation in a high time-resolution mode [14]. As in Timepix, high spatial resolution generally requires a large number of reading anodes in pixel-wise readout methods. A drastic reduction in the number of reading anodes has been achieved by using a delay-line readout in a $\mathrm{Gd_2O_3}$-doped neutron-sensitive MCP [15]. Orthogonal delay-line anodes are used to determine the X and Y coordinates of the neutron incident point. The delay-line MCP detector has a resolution of 65.6 μm and 63.7 μm for the X and Y directions, respectively, with a detection rate tolerance of 600 kHz. Because a single wire covers the entire X (or Y) spatial positioning on the delay line, its spatial resolution and detection-rate tolerance are determined by the temporal resolution of the time-stamp measurement and the signal resolution time: the advantage of this method is that it reduces the number of signal-reading lines by sacrificing the detection-rate tolerance. However, with fast timing recording, together with the fast rise and decay time of the signal, the detection-rate tolerance may improve. A typical neutron imager comprises a converter for converting neutrons to charged particles and/or to x rays, together with an appropriate detector. After conversion of the particles, the key to an improved imager is to find the effective detection method. A superconducting detector is one such detector with high sensitivity to charged particles and x rays. The high sensitivity for photons of various wavelengths has been demonstrated in a superconducting-nanowire single-photon detector [16], a transition-edge sensor (TES) [17], and a microwave kinetic-inductance detector [18,19]. Recently, a TES with a boron neutron-converter layer has been proposed to be used as a neutron detector [20]. A superconducting tunnel junction with a $\mathrm{Li_2B_4O_7}$ neutron-converter layer is also applicable for detecting neutrons [21,22].

We have been developing superconducting neutron detectors aimed at developing an improved neutron imager with higher spatial and energy resolutions by including a time-of-flight neutron source [23–27]. We succeeded in detecting neutrons by using a current-biased transition-edge detector (CBTED). We detected the local superconducting—normal transition of a ^{10}B-doped $\mathrm{MgB_2}$ meander line owing to a subtle change in the bias current induced by the nuclear reaction between an incident neutron and a ^{10}B nucleus [24]. The sensitive temperature range of the CBTED is limited to within 1% of the superconducting transition temperature T_c [28], which makes operation of this detector rather difficult. The current-biased kinetic-inductance detector (CBKID) works over a wide temperature range below T_c under a weak dc-biased current I_b. The current can be considerably lower than the superconducting critical current because it detects a time derivative of the kinetic inductance L_k in the superconducting state [25]. A photon detector based on a similar principle has also been reported previously [29]. Recently, we successfully detected neutron-incidence events by a CBKID method, wherein a superconducting Nb meander line and a ^{10}B neutron-capture layer were used [25,26]. We developed a multichannel Nb-based CBKID to utilize a neutron imager and determined the neutron-incidence position with < 1.3-mm accuracy in one dimension [27]. The feasibility of a high-spatial-resolution neutron imager has been extensively studied by developing an alternative method of fabricating a single-flux-quantum-(SFQ-)

integrated readout circuit [30]. The delay-line method is a promising technique to achieve high-resolution imaging without using multichanneling. In this paper, we demonstrate the feasibility of a delay-line CBKID imaging system in two dimensions. The developed system comprises the minimum number of signal wires (two) for two-dimensional position detection with capability suited for time-of-flight (TOF) neutron imaging. Our detector comprises an orthogonal set of superconducting Nb meander lines and a superimposed, enriched-^{10}B neutron-conversion layer. Neutron images are reproduced from the signal quartet detected at the four ends of the two sets of Nb meander lines. The energy resolution is achieved by the TOF method of pulsed neutrons.

II. BASIC FUNCTIONAL PRINCIPLE OF CBKID

A. Basic principles for signal generating

The signal-generating principle of a CBKID is distinctive because it only probes the time derivative of the kinetic inductance L_k in a superconducting wire. It senses very fast electronic phenomena such as the Cooper-pair-breaking process, but it is relatively insensitive to the recombination process thereafter. The kinetic inductance L_k is written as

$$L_k = \frac{m_s l}{n_s q_s^2 S}, \tag{1}$$

where m_s is the effective mass of the Cooper pair, q_s is the electric charge of the Cooper pair, n_s is the Cooper-pair density, l is the length of the stripline, and S is the cross-sectional area of the stripline. The transient change in L_K induced by the rapid reduction of n_s occurs locally at a hot spot within a tiny segment of the stripline over the length $\Delta l(\lll l)$ induced by the charged particles created from the $^{10}\mathrm{B} + n$ reaction. The relation between the transient change in L_k and the voltage V across the hot spot is expressed as

$$V = I_b\left(\frac{dL_k}{dt} + \frac{dL_m}{dt}\right) + (L_k + L_m)\frac{dI_b}{dt} \simeq I_b\frac{dL_k}{dt}, \tag{2}$$

where the magnetic inductance L_m is kept constant and $dI_b/dt \simeq 0$ as long as the detector remains in the superconducting state. Although Eq. (2) is in a spatially integrated form, a local hot spot from the neutron origin results in a locally diminished superconducting carrier density n_s and the singularity starts to propagate along the stripline.

B. Basic equation for signal propagation

The electrodynamics of a superconducting-nanowire system was calculated by Koyama and Ishida [31]. In our detector, assume that the superconducting waveguide has an S-I-S structure, the superconducting nanowire has a thickness of s (less than the London penetration depth λ_L), and the insulating layer has a few-hundred-nm thickness d.

A voltage pulse is created by a transient change in L_k at the hot spot, which propagates along the superconducting meander line with the wave dynamic equation for the phase difference $\theta(x,t)$ as follows:

$$\frac{1}{v(x,t)^2}\partial_t^2\theta(x,t) - \partial_x^2\theta(x,t) - \gamma(x,t)\partial_t\partial_x^2\theta(x,t) = F(x,t), \tag{3}$$

where the phase velocity v is obtained from

$$v(x,t) = \frac{c}{\sqrt{\epsilon}}\sqrt{\frac{d}{d + \lambda_L[1 + \coth(s/\lambda_L)/\zeta(x,t)]}}, \tag{4}$$

where $\zeta(x,t) = n_s(x,t)/n_s$ is the normalized superconducting density. Because $\zeta \approx 1$ is outside the hot spot, the velocity for the local excitation along the stripline is constant. $\gamma(x,t)$ is the relaxation time of the phase mode, given by

$$\gamma(x,t) = \frac{4\pi\sigma\lambda_L^3}{c^2\zeta(x,t)(\lambda_L + d)\coth(s/\lambda_L)}, \tag{5}$$

where σ is an Ohmic quasiparticle conductivity and the function $F(x,t)$ has a finite value only inside the hot spot, confined in a small spatiotemporal region. $F(x,t)$ acts as a source of the electromagnetic excitations propagating along the waveguide as the Swihart pulse [32]. As proved experimentally, the quasiparticle dissipation (γ) must be very small to ensure the long-distance transport of the signals when the detector is used at temperatures much lower than T_c. Detailed studies of these electrodynamics were published elsewhere [31].

C. Identification of the signal quartet

Signal polarity is primarily dominated by the flow direction of the dc-bias current along the stripline. A negative pulse propagates in the same direction as that of the dc-bias current flow, whereas a positive pulse propagates in the opposite direction [31]. Therefore, we can reasonably assign the signal polarity in each channel, as denoted in Fig. 1(a). When the neutron-incidence event occurs at an certain elapsed time t_0 from the reference time, we can estimate t_0 as

$$t_0 = \frac{t_{\mathrm{Ch4}} + t_{\mathrm{Ch3}}}{2} - \frac{l}{2v_x} = \frac{t_{\mathrm{Ch2}} + t_{\mathrm{Ch1}}}{2} - \frac{l}{2v_y}, \tag{6}$$

where t_{Ch1}, t_{Ch2}, t_{Ch3}, and t_{Ch4} are the time stamps of the signals received at Ch1, Ch2, Ch3, and Ch4, respectively, which correspond to the signals propagated toward both

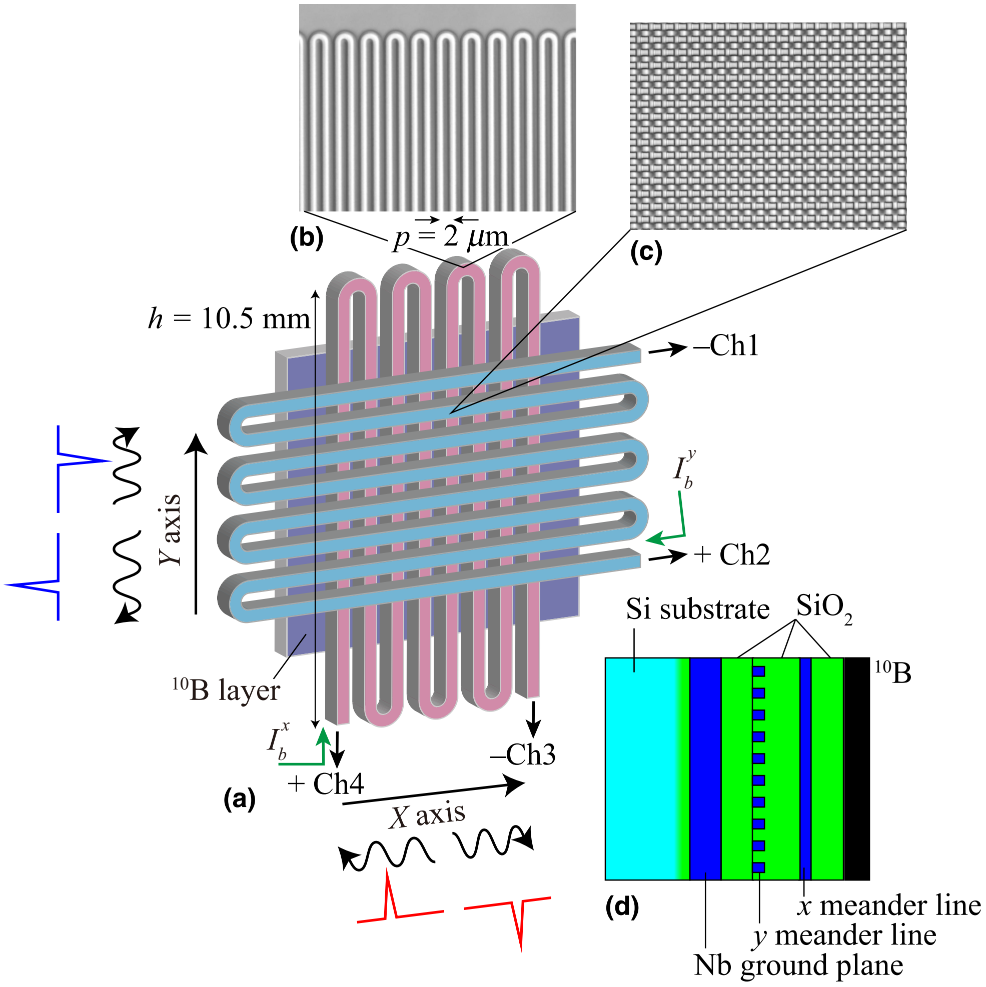

FIG. 1. (a) Schematic of the CBKID system. An X CBKID meander is orthogonal to a Y CBKID meander. The ^{10}B conversion layer is deposited on the CBKID system. Bias currents I_b^x and I_b^y are fed to the X and Y meander lines independently by constant dc voltage sources through 10-kΩ resistors. Both ends of the two meander lines are connected to the channels, Ch1, Ch2, Ch3, and Ch4, of a Kalliope-dc readout circuit. One pair, the positive and the negative pulses from the X detector, is measured by Ch4 and Ch3. The other pair, the positive and the negative pulses from the Y detector, is measured by Ch2 and Ch1. Laser microscope images exhibit (b) rounded turning points to ensure smooth signal transmission and (c) the regular intersections of the XY meanders. The pitch of the meander p (2 μm) and the length of meander segment h (10.5 mm) are indicated in the figure. (d) Schematic cross-sectional image of the XY CBKID system.

ends of the X (Ch3, Ch4) and Y (Ch1, Ch2) meander lines, respectively. l (52.5 m) is the total length of the meander line while v_x and v_y are the propagation velocities for the X and Y meander lines, respectively. It is noteworthy that t_0 can be determined independently in the X and Y meander lines. If the signals appearing on Ch1, Ch2, Ch3, and Ch4 originate from the same hit event, the elapsed time t_0 in the X and Y meander lines should coincide. This coincidence is the criterion to select a genuine combination of a signal quartet in our measurement, even if several signals exist simultaneously on a meander line. Therefore, a CBKID has a good multihit tolerance if the readout circuit is high speed enough. After identifying the signal quartet, the neutron-incidence position X and Y is determined as

$$X = \mathrm{ceil}\left\{\frac{(t_{\mathrm{Ch4}} - t_{\mathrm{Ch3}})v_x}{2h}\right\}p, \tag{7}$$

$$Y = \mathrm{ceil}\left\{\frac{(t_{\mathrm{Ch2}} - t_{\mathrm{Ch1}})v_y}{2h}\right\}p, \tag{8}$$

where h is the length of a single microstrip segment and p is the repetition pitch for the meander line. The spatial resolution is predominantly limited by the timing resolution of the measurement. The function “ceil” converts the signal-propagation length along the meander to the number of turns in the meander lines used for signal traveling. The acquired data are processed according to the abovementioned procedures on a data-processing computer to obtain a neutron transmission image.

III. DETECTOR DESIGN AND EXPERIMENTAL SETUP

A. Detector design

Figure 1 shows the schematic of our delay-line CBKID system. An enriched-^{10}B neutron-absorption layer is superimposed on top of the X and Y meander lines, which are orthogonal to each other in the line segment direction. A laser microscope image of the X meander line in Fig. 1 shows that all the turning points are rounded to ensure smooth propagations of the electromagnetic waves along the whole meander line. We also note that the meander-line width is kept constant including in the turning section. The rounded turning points are intended to reduce the reflection of the pulsed signals from the unmatched impedance over the whole meander line. In the middle panel of photos, the overwrapping region of the X and Y meander lines is shown. The ultimate pixel size of our detector is defined by the repetition period of the microstrip lines, whereas the actual pixel size is an integral multiple of the repetition period because the signals propagate along a few turns of the meander lines within the resolution time. The address of the pixels may be identified by the one-dimensional locations of the X and Y meander lines. Because the timing resolution of our system is 1 ns at best and the signal-propagation speed components v_x and v_y are approximately 1/3 of the speed of light, the minimum distance we can identify along the meander lines is $10^8 \times 10^{-9} = 0.1$ m. This is about five turns of our meander lines in both the X and Y directions. Both the X and Y superconducting Nb striplines of 1-μm width are folded to meander lines every $h = 10.5$ mm with a spacing of 1 μm. The repetition period is $p = 2$ μm and the total length of the meander line extends to $l = 52.5$ m.

Seven layers are deposited on a thermally oxidized Si substrate in our stacked detector, as schematically shown in Fig. 1(d). They are stacked sequentially from bottom to top as follows: (1) a silicon substrate of 625-μm thickness, (2) a 300-nm-thick SiO_2 layer, (3) a superconducting Nb ground plane of 300-nm thickness, (4) a passivation SiO_2 layer of 250-nm thickness, (5) a superconducting 40-nm-thick Nb Y meander line, (6) a passivation SiO_2 layer of 300-nm thickness, (7) a superconducting 40-nm-thick Nb X meander line, (8) a passivation SiO_2 layer of 250-nm thickness, and (9) an enriched-^{10}B neutron-capture layer of 300-nm thickness. The sensitivity of the CBKID to γ rays is negligibly small because of the low absorption probability of the constituent materials and the small effective thickness of the Nb meander line for γ rays. The Nb meander line with two end electrodes is fabricated in the Clean Room for Analog-Digital-Superconductivity (CRAVITY) at the National Institute of Advanced Industrial Science and Technology (AIST). The ^{10}B layer is deposited on the meander using a molecular beam technique under an ultrahigh vacuum of 10^{-7} Pa at Osaka Prefecture University.

B. Readout diagram

The dc-bias currents I_b^x and I_b^y are applied by two constant voltage sources through 10 kΩ resistors for both of the meander lines. Equation (2) is convenient for users, because the output signal V can be tuned by adjusting the amplitude of the bias current I_b. A pair of pulsed signals is initiated by a local transient change in n_s, and the pulses propagate toward the two ends of the strip line (meander line). The signals are amplified by an ultralow-noise amplifier (SA-430 F5 by NF Corporation) and are detected by a 2.5-GHz-sampling digital oscilloscope (Teledyne LeCroy HDO4104-MS) and a Kalliope-dc readout circuit. The Kalliope-dc readout circuit has a 1-ns-sampling multichannel time-to-digital converter (TDC), which was originally developed by Kojima *et al.* for muon-spin relaxation (μSR) measurements at the J-PARC facility [33]. The original Kalliope readout circuit has a time window of the first 64 μs and subsequently transfers data to the storage in the remaining 40 ms, which is long enough to handle all the data traffic in muon experiments. In the present work, we extend the time window to 4.2 s by increasing the bit width of the TDC from 16 to 32 bits. Also, we modify the firmware in the field-programmable gate-array unit of Kalliope to ensure that the data transfer is performed immediately after event detection. Thanks to this modification, the time-stamp measurements of 1-ns temporal resolution over a time window up to 4.2 s without any dead time before and after data acquisition are possible, which is more than enough to cover the neutron-pulse repetition period of 40 ms at J-PARC. The data-acquisition process is restarted for every pulse to be synchronous to neutron creation, because the timing signal of the neutron creation is used as the start signal of the readout circuit. When the analog input exceeds the threshold voltage, a stop signal for TDC is triggered. The voltage thresholds used to evaluate the time stamps of the analog inputs can be tuned independently in the four channels. The time-stamp data are transferred to a data-acquisition computer by using the SiTCP protocol [34] simultaneously upon producing stop signals.

C. Cooling the detector and experimental

In a low-temperature (< 4 K) cryostat, heat leak via a number of signal leads often causes dissipation of the cooling power and a rise in the lowest attainable temperature, which is a hindrance for keeping a high-spatial-resolution, two-dimensional superconducting detector below T_c. One promising solution is the delay-line method. Our delay-line CBKID imager requires only four leads for the signal readout even though it works as a high-spatial-resolution neutron imager, which proves to be an advantage considering that the incoming heat flux flows through fewer electrical leads. Our neutron detector is cooled down to 4 K by using a Gifford-McMahon (GM) refrigerator, which is suitable for long-time data acquisition. The mechanical vibration of the system is suppressed by an antivibration cryostat. The size of the cryostat is roughly 300 mm in diameter and 820 mm in height, as shown in Fig. 2(a). A photograph of the cryostat in the irradiation chamber is shown in Fig. 2(b). The detector and test pattern are mounted on the detector stage in the cryostat 207 mm from the bottom. The vacuum can and the main parts of the detector holder are made from an aluminum alloy to ensure transparency for the neutron beam. The neutron beam is irradiated to the detector from the substrate side through the test pattern, which is placed at a distance of 0.8 mm from the detector, as illustrated in Fig. 2(c) as a “metal mesh,” and cooled

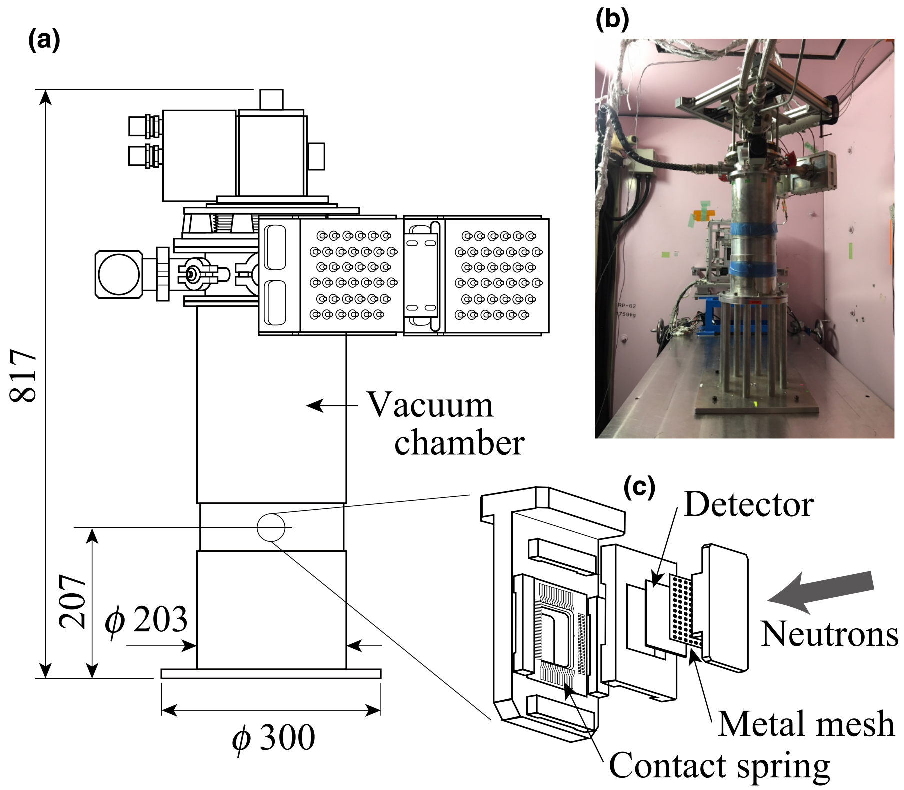

FIG. 2. (a) A schematic overview of the Gifford-McMahon (GM) refrigerator and (b) photograph of the irradiation chamber. (c) A schematic overview of the detector and metal-mesh setup. The neutrons are incident from the substrate side.

down with the detector. Electrical contact springs are used to connect the detector. Neutron-irradiation experiments are performed with pulsed neutrons with the collimator ratio $L/D = 14\ \mathrm{m}/0.1\ \mathrm{m} = 140$ at BL10 of the Material and Life Science Experimental Facility (MLF), J-PARC [35]. The energy resolution is achieved by the TOF method through the 14-m flight path of the facility with 33 μs full width at half maximum (FWHM) at 10 meV.

IV. RESULTS AND DISCUSSION

A. Cold signal-propagation velocity measurements without neutrons

The stability and accuracy of the signal-propagation velocity have a significant influence on the spatial resolution while applying the delay-line CBKID method to neutron radiography. To measure propagation velocity, we apply a short pulse signal from a function generator to one end of the 52.5-m-long meander wire. Because the meander line acts as a superconducting strip line, the signal easily reaches the other end of the long meander line. We observe a transmitted signal by using a digital oscilloscope with a sampling period of 0.4 ns. A Cernox thermometer is placed in the vicinity of the cryogenic CBKID system. The detector temperature is controlled at 4.15 K by using a temperature controller and is monitored for the entire duration of the measurements. We confirm that the propagation velocities are stable enough within ±0.1% over a 7-h period, whereas the detector temperature is controlled at a temperature between 4.13 and 4.17 K. We notice that the two different values of each velocity are not real but simply arise due to a final digit in the time base of our oscilloscope. Thus, we conclude that the propagation velocities for the X and Y meander lines are stable enough to conduct a reliable imaging experiment over a long accumulation time at 4.15 K.

B. Signal quartet on the meander line induced by a neutron hit event

In Fig. 3, we show a typical signal quartet. Ch1 and Ch2 correspond to both ends of the Y meander line, whereas Ch3 and Ch4 correspond to both ends of the X meander. Note that the signal polarities are opposite to each other as previously mentioned in Sec. II C. We consider that these four different signals arise from the single-neutron-reaction event at the hot spot, as it follows the criterion of Eq. (6). The signal-pair components on one meander line have the same amplitude but with opposite polarities when they are created at the hot spot. The signal heights in each pair are almost the same, although they are influenced by the signal attenuation depending on the propagation distance. We note that an averaged signal height is remarkably different for the X and Y meander lines when I_b^x and I_b^y are kept identical and the reason for the discrepancy remains to be studied. Before the imaging measurement, we tune the signal amplitude by adjusting the X and Y biasing currents such that an averaged signal height is comparable within the two detectors. We choose

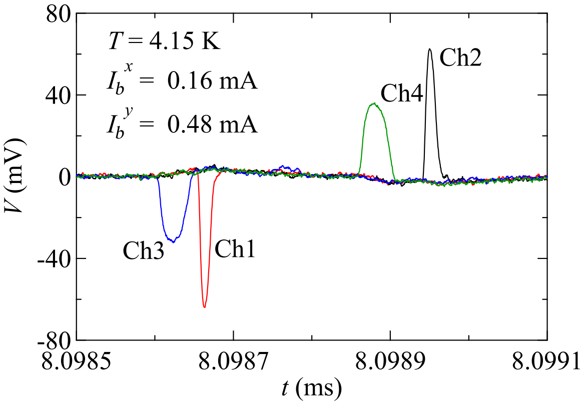

FIG. 3. Typical signals from Ch1 (red), Ch2 (black), Ch3 (blue), and Ch4 (green) at $T = 4.15$ K. Here, note that the neutrons are generated at $t = 0$ ms. Ch4 and Ch3 represent a pair: the positive and negative pulses from the X detector fed by the bias current $I_b^x = 0.16$ mA. Ch2 and Ch1 are another pair: the positive and negative pulses from the Y detector fed by $I_b^y = 0.48$ mA.

bias currents of $I_b^x = 0.16$ mA and $I_b^y = 0.48$ mA. The signal widths observed from the X meander in Ch3 and Ch4 are a few times wider than those from the Y meander in Ch1 and Ch2, but they are still within the order of a few tens of ns. These widths enable high-speed measurements and energy-dispersive neutron imaging with the combination of the TOF technique in a pulsed neutron source. We estimate the detection-rate tolerance to be as high as a few tens of MHz because CBKIDs can handle multihit events.

C. Energy-integrated neutron imaging and spatial resolution

To evaluate the spatial resolution of our CBKID imaging system experimentally, we conduct a neutron-imaging demonstration by using a well-shaped neutron absorber as a test pattern. The test absorber comprises a 50-μm-thick stainless-steel mesh (15×15 mm^2 in size), wherein 100×100-μm^2 square holes are arrayed in a square lattice (lattice constant 250 μm). Each hole is tightly filled by very fine ^{10}B particles. Because the stainless mesh is fabricated by a wet etching technique, the corners and edges of the square hole are somewhat rounded [see an optical photograph shown in Fig. 4(b)]. In Fig. 4(a), we show the neutron-radiography image of the ^{10}B dot array, which matches the photo image of the test pattern. Measurements are performed at $T = 4.15$ K with $I_b^x = 0.16$ mA and $I_b^y = 0.48$ mA for 30.4 h at 200-kW beam power with an incident neutron wavelength λ ranging from 0.05 to 1.13 nm. We reconstruct a neutron image from the corrected-signal detecting times in Ch1, Ch2, Ch3, and Ch4 by using Eqs. (7) and (8). The color scale indicates the number of events (NOE) over 30.4 h. The hole size and repetition period are estimated from the neutron imaging as 106 and 249 μm, respectively, in the Y direction, whereas, in the X direction, they are 111 and 244 μm, respectively. The hole size and repetition are in fairly good agreement with the 100×100-μm^2 hole and the pitch of 250 μm in the metal mesh.

Here, we discuss the spatial uncertainties δX and δY expected from those in the propagation velocities (δv) and the time stamps (δt). Following the regular expression for error propagation, δX is expressed as

$$X \pm \delta X = \frac{p(t_{\mathrm{Ch4}} \pm \delta t_{\mathrm{Ch4}} - t_{\mathrm{Ch3}} \mp \delta t_{\mathrm{Ch3}})(v_x \pm \delta v_x)}{2h},$$

$$\delta X \simeq \frac{\delta v_x}{v_x} x + \frac{p v_x}{2h} \delta t_x, \tag{9}$$

$$\delta t_x = \delta t_{\mathrm{Ch4}} + \delta t_{\mathrm{Ch3}}, \tag{10}$$

where δt_{Ch3} and δt_{Ch4} are the measurement errors of the detecting times in Ch3 and Ch4, respectively, and δv_x is

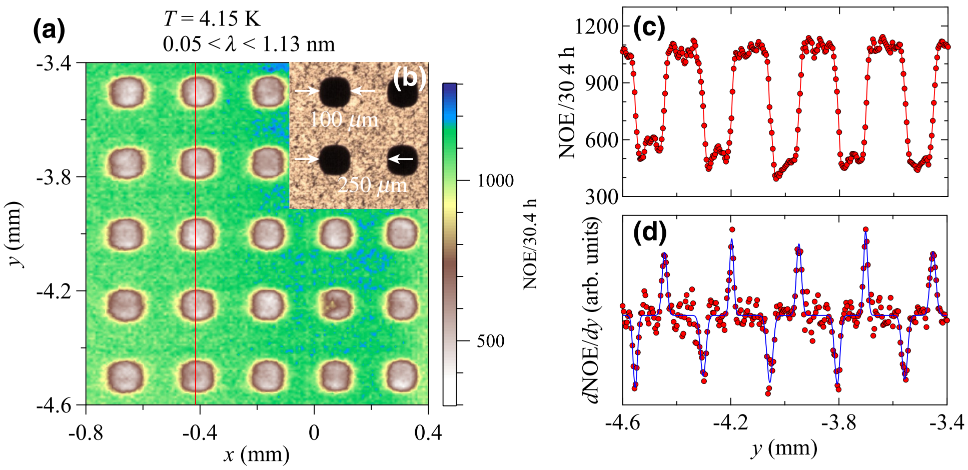

FIG. 4. (a) Neutron-radiography imaging of the ^{10}B dot array contained in the stainless-steel mesh. Neutrons with the neutron wavelength λ ranging from 0.05 to 1.13 nm are used to construct the image. (b) An optical photograph of the test absorber, which comprises a 50-μm-thick stainless-steel mesh. Each hole is tightly filled by very fine ^{10}B particles. (c) The number of events (NOE) along the red line in the image in the 300×300 bin area for 30.4 h. (d) Numerical differentiation of NOE as a function of y [see the red line of (a)]. The solid line is a fit to a Gaussian function to highlight the ^{10}B dot boundary.

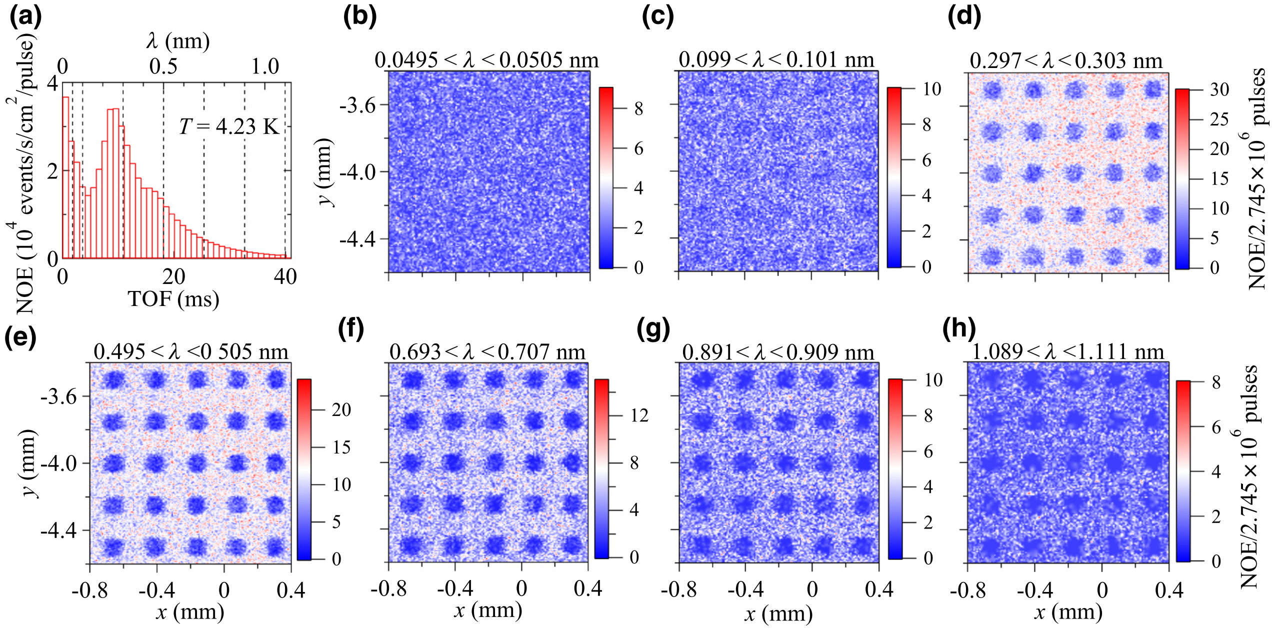

FIG. 5. (a) The histogram of the NOE per histogram bin per detector area per pulse as a function of time of flight t or wavelength λ. Black dotted lines correspond to the imaging wavelengths of $\lambda = 0.05$, 0.1, 0.3, 0.5, 0.7, 0.9, and 1.1 nm. Two-dimensional images of the neutron absorber recovered by neutrons are shown for several different wavelengths: (b) $0.0495 < \lambda < 0.0505$ nm, (c) $0.099 < \lambda < 0.101$ nm, (d) $0.297 < \lambda < 0.303$ nm, (e) $0.495 < \lambda < 0.505$ nm, (f) $0.693 < \lambda < 0.707$ nm, (g) $0.891 < \lambda < 0.909$ nm, and (h) $1.089 < \lambda < 1.111$ nm.

the measurement error in the propagation velocity in the X meander line. Similarly,

$$\delta Y \simeq \frac{\delta v_y}{v_y} y + \frac{p v_y}{2h} \delta t_y, \tag{11}$$

$$\delta t_y = \delta t_{\mathrm{Ch2}} + \delta t_{\mathrm{Ch1}}, \tag{12}$$

where δt_{Ch1} and δt_{Ch2} are the measurement errors of the detecting times in Ch1 and Ch2, respectively, and δv_y is the measurement error in the propagation velocity in the Y meander line. We estimate $\delta v_x/v_x$ and $\delta v_y/v_y$ to be 1.29×10^{-5} and 1.26×10^{-5}, respectively. In the evaluation of the maximum value of $x = y = 5$ mm, the first term of Eqs. (9) and (11), namely, the positional error due to the uncertainty of the speed, is only approximately 6×10^{-2} μm, which is negligibly small. Therefore, the second term in Eqs. (9) and (11), i.e., the uncertainty of the time measurement, is the dominant source of the positional error. If we assume δt_x and δt_y are the same with the timing resolution of TDC of 1 ns, the corresponding positional errors are $\delta X = p v_x \delta t_x / 2h = 8.8$ μm and $\delta Y = p v_y \delta t_y / 2h = 7.1$ μm. We note that δY is smaller than δX because v_y is notably slower compared with v_x. The hole size and period as determined by neutron imaging are all within the estimated errors, except for the size in the X direction (111 ± 8.8-μm measurement vs. 100-μm test pattern), but the discrepancy is small.

Figure 4(c) shows a line profile along the red line in Fig. 4(a). We estimated the sharpness of the dot boundary of the FWHM of each peak in the derivation shown by the blue lines in Fig. 4(d). Averages of FWHM are less than 22 and 41 μm in the Y and X directions, respectively, which is 3–5 times worse than the spatial uncertainty from the TDC resolution. Higher spatial resolution in the Y direction compared with that in the X direction is, again, consistent with a slower propagation velocity along the Y meander line compared with that along the X meander line. We note that the origin of the error is partially due to the rounding of the etched edges of the holes in the metal mesh. Also, the time stamp determination from the fixed threshold voltage for the analog pulse may involve a timing jitter and result in the pulse-height distribution.

D. Energy-resolved neutron imaging

In Fig. 5(a), the time distribution of detection events in the delay-line CBKID is shown. The characteristic TOF or λ dependence of the neutron flux [36] is well reproduced. Here, we note that the delay-line CBKID has the capability of high-energy resolution because of the sufficiently high timing resolution of our system. The neutron wavelength λ is proportional to the TOF and the neutron energy E as λ (nm) $= 28.2556 \times t$ (s) $= 0.9044/\sqrt{E}$ (eV) at BL10.

To demonstrate the high neutron-energy resolution, we show the neutron images from seven different λ as discriminated by the dotted lines in Fig. 5(a) with the width of $\Delta\lambda/\lambda = \pm 1\%$. Figures 5(b)–5(h) present the neutron imaging of the test pattern corresponding to each wavelength. The color scale indicates the NOE. We succeed in obtaining clear neutron images. Figure 5(b), which has the image for the $\lambda \simeq 0.05$ nm slice, exhibits an unclear pattern of the mask compared with Fig. 5(c), which shows the $\lambda \simeq 0.1$ nm slice. This observation is consistent with the fact that the ^{10}B neutron-absorption cross section becomes lower at shorter wavelengths. As discussed above, we demonstrate that the delay-line CBKID can be used for neutron-wavelength-resolved imaging owing to the high temporal resolution of the Kalliope-dc readout circuit.

E. Detection efficiency

Detection efficiency is one of the important performance indicators of neutron detectors. The present detector has a 300-nm-thick ^{10}B neutron-capture layer, indicating that the detection efficiency for $\lambda = 0.6$ nm is less than 3%. By comparison with our previous report [26] and the ^{10}B thickness, the detection efficiency is approximately 1% in the present experiment. The detection efficiency is quite limited at the present stage because the system is under development. We plan to improve the detection efficiency by increasing the ^{10}B-layer thickness to 1 μm for promoting the nuclear reaction. One can expect a detection efficiency of 10% for $\lambda = 0.6$ nm as the maximum with a 1-μm-thick ^{10}B layer. Herein, we note that the 1-μm-thick ^{10}B layer is probably the most efficient because the efficiency for a CBKID with an excessively thick neutron-conversion layer worsens due to the limitation of the mean range of ions. For further improvement of the efficiency, multiple stacking of the detector is worth considering.

V. SUMMARY

We provide a clear demonstration that the delay-line CBKIDs can be used for energy-dispersive neutron imaging in combination with the Kalliope-dc readout circuit with 1-ns-resolution TDC for high-speed data acquisition without losing any pulse of the pulsed neutrons from the MLF facility of J-PARC. Clear images of the ^{10}B neutron-absorber dot array are observed, because we avoid the blurring effect due to the beam divergence by placing the test pattern at a vicinity distance of 0.8 mm from the X/Y CBKID detectors. The energy-integrated spatial resolution successfully reached 22 μm in the Y direction and 41 μm in the X direction, without performing any numerical corrections after data processing. The signal-pulse width of a few tens of nanoseconds implies that the detection-rate tolerance can reach up to a few of tens of MHz. It is crucial for a superconducting detector to reduce the number of signal leads to four by employing an X/Y delay-line technique for decreasing the heat flux from room temperature to the cryogenic temperature. This is also useful for us to realize high-resolution imaging with a small-sized cryocooler. The delay-line CBKID system has the merit of determining the image resolution afterward: one can construct any pixel sizes by employing proper rebinning to construct images. The role of a meander line in this system is not only to receive ions emitted by a nuclear reaction but also to act as the delay-line detector. Therefore, expanding the active area of the detector does not ruin but actually helps the spatial resolution because of a simple extension of the meander segment length (h). Further improvements in spatial resolution can be achieved in principle without further difficulty by shortening the meander-line pitch (p) using a higher-temporal-resolution readout circuit and expanding the length (h) of the meander segment.

ACKNOWLEDGMENTS

This work is partially supported by a Grant-in-Aid for Scientfic Research (S) (Grant No. 23226019) and (A) (Grant No. 16H02450) from JSPS. The neutron-irradiation experiments at the Materials and Life Science Experimental Facility (MLF) of the J-PARC are conducted under the support of MLF programs (Proposals No. 2015A0129 and No. 2015P0301). This work is supported by the Cadence software of VDEC at the University of Tokyo. Development of Kalliope TDC and readout electronics/software is conducted under the collaboration of KEK Open Source Consortium of Instrumentation (Open-IT).

[1] N. Kardjilov, I. Manke, A. Hilger, M. Strobl, and J. Banhart, Neutron imaging in materials science, Mater. Today **14**, 248 (2011).

[2] A. S. Tremsin, J. Rakovan, T. Shinohara, W. Kockelmann, A. S. Losko, and S. C. Voge, Non-destructive study of bulk crystallinity and elemental composition of natural gold single crystal samples by energy-resolved neutron imaging, Sci. Rep. **7**, 40759 (2017).

[3] R. Satija, D. L. Jacobson, M. Arif, and S. A. Werner, In situ neutron imaging technique for evaluation of water management systems in operating PEM fuel cells, J. Power Sources **129**, 238 (2004).

[4] J. B. Siegel, A. G. Stefanopoulou, P. Hagans, Y. Ding, and D. Gorsich, Expansion of lithium ion pouch cell batteries: Observations from neutron imaging, J. Electrochem. Soc. **160**, A1031 (2013).

[5] E. H. Lehmann, P. Vontobel, E. Deschler-Erb, and M. Soares, Non-invasive studies of objects from cultural heritage, Nucl. Instrum. Methods Phys. Res. A **542**, 68 (2005).

[6] R. Woracek, J. Santisteban, A. Fedrigo, and M. Strobl, Diffraction in neutron imaging—A review, Nucl. Instrum. Methods Phys. Res. A **878**, 141 (2018).

[7] M. Matsubayashi, A. Faenov, T. Pikuz, Y. Fukuda, and Y. Kato, Neutron imaging of micron-size structures by color center formation in LiF crystals, Nucl. Instrum. Methods Phys. Res. A **622**, 637 (2010).

[8] S. H. Williams, A. Hilger, N. Kardjilov, I. Manke, M. Strobl, P. A. Douissard, T. Martin, H. Riesemeier,

and J. Banhart, Detection system for microimaging with neutrons, J. Instrum. **7**, P02014 (2012).

[9] P. Trtik and E. H. Lehmann, Progress in high-resolution neutron imaging at the Paul Scherrer Institut – The neutron microscope project, J. Phys. Conf. Ser. **746**, 0120 (2016).

[10] D. S. Hussey, J. M. LaManna, E. Baltic, and D. L. Jacobson, Neutron imaging detector with 2 μm spatial resolution based on event reconstruction of neutron capture in gadolinium oxysulfide scintillators, Nucl. Instrum. Methods Phys. Res. A **866**, 9 (2017).

[11] A. S. Tremsin, J. B. McPhate, J. V. Vallerga, O. H. W. Siegmund, W. B. Feller, E. Lehmann, L. G. Butler, and M. Dawson, High-resolution neutron microtomography with noiseless neutron counting detector, Nucl. Instrum. Methods Phys. Res. A **652**, 400 (2011).

[12] A. S. Tremsin, J. V. Vallerga, J. B. McPhate, and O. H. W. Siegmund, Optimization of high count rate event counting detector with Microchannel Plates and quad Timepix readout, Nucl. Instrum. Methods Phys. Res. A **787**, 20 (2015).

[13] X. Llopart, R. Ballabriga, M. Campbell, L. Tlustos, and W. Wong, Timepix, a 65k programmable pixel readout chip for arrival time, energy and/or photon counting measurements, Nucl. Instrum. Methods Phys. Res. A **581**, 485 (2007).

[14] T. Poikela, J. Plosila, T. Westerlund, M. Campbell, M. De Gaspari, X. Llopart, V. Gromov, R. Kluit, M. van Beuzekom, and F. Zappond, Timepix3: A 65K channel hybrid pixel readout chip with simultaneous ToA/ToT and sparse readout, J. Instrum. **9**, C05013 (2014).

[15] Y. Wang, Y. Yang, X. Wang, and Y. Li, Readout for a large area neutron sensitive microchannel plate detector, Nucl. Instrum. Methods Phys. Res. A **784**, 226 (2015).

[16] C. M. Natarajan, M. G. Tanner, and R. H. Hadfield, Superconducting nanowire single-photon detectors: Physics and applications, Supercond. Sci. Technol. **25**, 063001 (2012).

[17] K. D. Irwin, An application of electrothermal feedback for high resolution cryogenic particle detection, Appl. Phys. Lett. **66**, 1998 (1995).

[18] P. K. Day, H. G. LeDuc, B. A. Mazin, A. Vayonakis, and J. Zmuidzinas, A broadband superconducting detector suitable for use in large arrays, Nature **425**, 817 (2003).

[19] J. Zmuidzinas, Superconducting microresonators: Physics and applications, Annu. Rev. Condens. Matter Phys. **3**, 169 (2012).

[20] V. Merlo, M. Salvato, M. Cirillo, M. Lucci, I. Ottaviani, A. Scherillo, G. Celentano, and A. Pietropaolo, Hybrid superconducting neutron detectors, Appl. Phys. Lett. **106**, 113502 (2015).

[21] T. Nakamura, M. Katagiri, M. Ukibe, T. Ikeuchi, and M. Ohkubo, Neutron detection by superconducting tunnel junctions on a $Li_2B_4O_7$ single-crystal absorber, Nucl. Instrum. Methods A **520**, 67 (2004).

[22] T. Nakamura, M. Katagiri, Y. E. Chen, M. Ukibe, and M. Ohkubo, Development of a neutron-imaging detector based on pulse-height correlation between two superconducting tunnel junctions on a $Li_2B_4O_7$ crystal, Nucl. Instrum. Methods A **559**, 766 (2006).

[23] K. Takahashi, K. Satoh, T. Yotsuya, S. Okayasu, K. Hojou, M. Katagiri, A. Saito, A. Kawakami, H. Shimakage, Z. Wang, and T. Ishida, Design of neutron detector by using a novel superconductor MgB_2, Physica C **392–396**, 1501 (2003).

[24] T. Ishida, M. Nishikawa, Y. Fujita, S. Okayasu, M. Katagiri, K. Satoh, T. Yotsuya, H. Shimakage, S. Miki, Z. Wang, M. Machida, T. Kano, and M. Kato, Superconducting MgB_2 thin film detector for neutrons, J. Low Temp. Phys. **151**, 1074 (2008).

[25] H. Shishido, S. Miyajima, Y. Narukami, K. Oikawa, M. Harada, T. Oku, M. Arai, M. Hidaka, A. Fujimaki, and T. Ishida, Neutron detection using a current biased kinetic inductance detector, Appl. Phys. Lett. **107**, 232601 (2015).

[26] S. Miyajima, H. Shishido, Y. Narukami, N. Yoshioka, A. Fujimaki, M. Hidaka, K. Oikawa, M. Harada, T. Oku, M. Arai, and T. Ishida, Neutron flux spectrum revealed by Nb-based current-biased kinetic inductance detector with ^{10}B conversion layer, Nucl. Instrum. Methods Phys. Res. A **842**, 71 (2017).

[27] H. Shishido, H. Yamaguchi, Y. Miki, S. Miyajima, K. Oikawa, M. Harada, M. Hidaka, T. Oku, M. Arai, A. Fujimaki, and T. Ishida, Neutron detection using the superconducting Nb-based current-biased kinetic inductance detector, Supercond. Sic. Technol. **30**, 094003 (2017).

[28] I. Yagi, N. Yoshioka, H. Shishido, T. Yotsuya, S. Miki, Z. Wang, and T. Ishida, Current-biased transition edge detector of MgB_2 nanowires for neutrons: Imaging by scanning laser, IEEE Trans. Appl. Supercond. **23**, 2200904 (2013).

[29] M. Lindgren, M. Currie, C. Williams, T. Y. Hsiang, P. M. Fauchet, and R. Sobolewski, Intrinsic picosecond response times of Y–Ba–Cu–O superconducting photodetectors, Appl. Phys. Lett. **74**, 853 (1999).

[30] A. Fujimaki, I. Nakanishi, S. Miyajima, K. Arai, Y. Akita, and T. Ishida, Proposal of a compact neutron diffraction system with a single-flux-quantum signal processor, IEICE Trans. Electron. **E94-C**, 254 (2011).

[31] T. Koyama and T. Ishida, Electrodynamic theory for the operation principle of a superconducting kinetic inductance stripline detector, J. Phys.: Conf. Ser. **1054**, 012055 (2018).

[32] J. C. Swihart, Field solution for a thin-film superconducting strip transmission line, J. Appl. Phys. **32**, 461 (1961).

[33] K. M. Kojima, T. Murakami, Y. Takahashi, H. Lee, S. Y. Suzuki, A. Koda, I. Yamauchi, M. Miyazaki, M. Hiraishi, H. Okabe, S. Takeshita, R. Kadono, T. Ito, W. Higemoto, S. Kanda, Y. Fukao, N. Saito, M. Saito, M. Ikeno, T. Uchida, and M. M. Tanaka, New μSR spectrometer at J-PARC MUSE based on Kalliope detectors, J. Phys.: Conf. Ser. **551**, 012063 (2014).

[34] T. Uchida, Hardware-based TCP processor for gigabit Ethernet, IEEE Trans. Nucl. Sci. **55**, 1631 (2008).

[35] K. Oikawa, F. Maekawa, M. Harada, T. Kai, S. Meigo, Y. Kasugai, M. Ooi, K. Sakai, M. Teshigawara, S. Hasegawa, M. Futakawa, Y. Ikeda, and N. Watanabe, Design and application of NOBORU—NeutrOn Beam line for Observation and Research use at J-PARC, Nucl. Instrum. Methods Phys. Res. A **589**, 310 (2008).

[36] Y. Harada, F. Maekawa, K. Oikawa, S. Meigo, H. Takada, and M. Fitakawa, Application and validation of particle transport code PHITS in design of J-PARC 1 MW spallation neutron source, Prog. Nucl. Sci. Technol. **2**, 872 (2011).